


Experimental Observations of Laser-Driven Tin Ejecta Microjet Interactions

A. M. Saunders^{1,*}, C. V. Stan¹, K. K. Mackay¹, B. Morgan¹, J. A. K. Horwitz¹, S. J. Ali¹, H. G. Rinderknecht^{1,2}, T. Haxhimali¹, Y. Ping¹, F. Najjar¹, J. Eggert¹, and H.-S. Park¹

¹Lawrence Livermore National Laboratory, 7000 East Avenue, Livermore, California 94550, USA

²Laboratory for Laser Energetics, University of Rochester, 250 East River Road, Rochester, New York 14623, USA

 (Received 16 April 2021; revised 3 July 2021; accepted 19 August 2021; published 5 October 2021)

The study of high-velocity particle-laden flow interactions is of importance for the understanding of a wide range of natural phenomena, ranging from planetary formation to cloud interactions. Experimental observations of particle dynamics are sparse given the difficulty of generating high-velocity flows of many particles. Ejecta microjets are micron-scale jets formed by strong shocks interacting with imprinted surfaces to generate particle plumes traveling at several kilometers per second. As such, the interaction of two ejecta microjets provides a novel experimental methodology to study interacting particle streams. In this Letter, we report the first time sequences of x-ray radiography images of two interacting tin ejecta microjets taken on a platform designed for the OMEGA Extended Performance (OMEGA EP) laser. We observe that the microjets pass through each other unattenuated for the case of 11.7 ± 3.2 GPa shock pressures and jet velocities of 2.2 ± 0.5 km/s but show strong interaction dynamics for 116.0 ± 6.1 GPa shock pressures and jet velocities of 6.5 ± 0.5 km/s. We find that radiation-hydrodynamic simulations of the experiments are able to capture many aspects of the collisional behavior, such as the attenuation of jet velocity in the direction of propagation, but are unable to match the full spread of the strongly interacting cloud.

DOI: [10.1103/PhysRevLett.127.155002](https://doi.org/10.1103/PhysRevLett.127.155002)

Interactions of high-velocity particle-laden flows are an area of active research in fields that seek to understand dynamics of pebble accretion in planetary formation [1–7], particle flow under turbulence [8–12], cloud interaction dynamics [13–15], and chemically reactive sprays [16,17]. When particles travel at velocities exceeding several kilometers per second, collisions between particles can impart enough energy to alter the material state of the particles through collisional melting or vaporization, in addition to altering flow velocities and particle sizes due to particle agglomeration and breakup. As such, interaction behavior of high-velocity particle flows is difficult to predict and requires experimental data to benchmark collisional models.

Thus far, experimental data on interactions of high-velocity particle-laden flows are sparse due to the difficulties in accelerating numerous counterpropagating particles at such velocities. An ejecta microjet forms when a shock breaks out from a free surface of a material that has a micron-scale surface perturbation, such as a groove or divot [18–26]. The perturbation inverts and can generate a micron-scale jet of material traveling at a velocity of several kilometers per second. A simplified model of jet evolution assumes that microjets break up through secondary instability processes into ligaments and eventually into fine particles or droplets [27–29]. As a result, the physics of particle-laden flow is often linked with the physics of jet evolution, and interactions of ejecta microjets provide a

novel experimental methodology to study interactions of high-velocity particle flows.

While extensive work has been performed to understand the properties governing microjet formation and evolution [24,30–41], collisions of interacting ejecta microjets have largely been neglected by researchers. In this Letter, we present the first measurements of interaction behavior between two high-velocity tin ejecta microjets as captured through sequences of x-ray radiography images from experiments on the OMEGA EP laser [42]. We measure that ejecta microjets from a tin shock pressure before release of 11.7 ± 3.2 GPa travel at velocities of 2.2 ± 0.5 km/s, while microjets from tin shocked at 116.0 ± 6.1 GPa travel at 6.5 ± 0.5 km/s. In addition, the jets from the 116.0 GPa drive show volume fractions of up to 5 times higher than those in the 11.7 GPa case. We observe that jets from the lower drive pressure pass through each other unattenuated, while jets from the higher drive pressure show strong interaction dynamics with the growth of a cloud centered around the interaction point. We perform simulations of particle collision dynamics using a hard-sphere collisional model and are unable to reproduce the spread of particles postcollision observed in the high-pressure shock. The observed discrepancies in the experimental data and the simulation predictions point to material effects or spatial inhomogeneities not captured in the simulations.

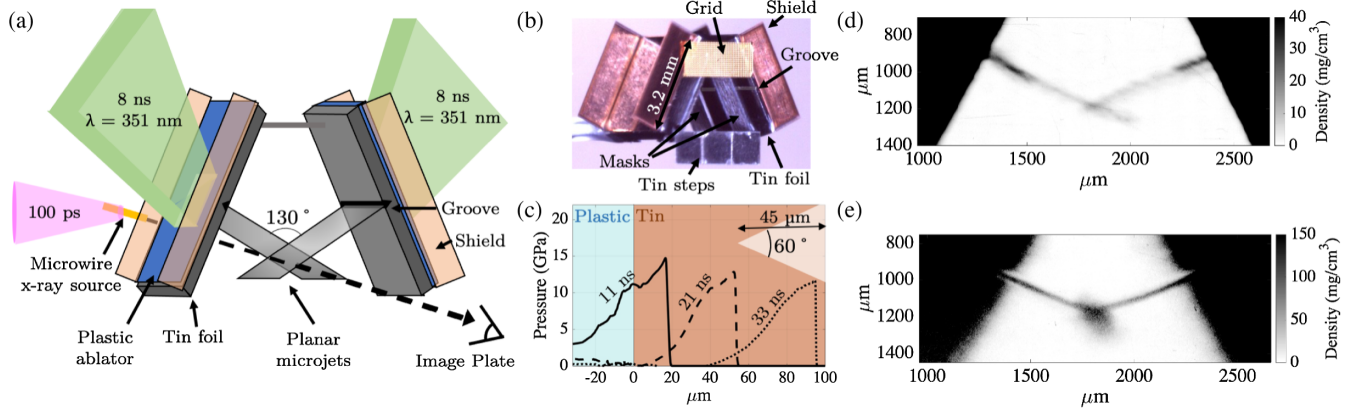


FIG. 1. (a) A schematic of the OMEGA EP laser platform used to drive tin microjets and collect x-ray radiography measurements of the jet interactions. Two long-pulse lasers drive shocks into tin foils with grooves carved into their rear surfaces. A short-pulse laser on a microwire target generates x rays for the radiography measurement. (b) A picture of the target indicating key elements and dimensions. Tin steps of known thicknesses allow calibration of the radiography diagnostic for density reconstruction. The shields are used to block the intense ablation-plasma emission from the radiography image plates. Masks are offset from the inner surfaces of the tin samples to limit the region of the jet that propagates to the interaction point. (c) Simulated spatial variations of pressure at three time instances, highlighting the decay of shock pressure through the tin sample. Groove schematic is overlaid on simulation results. (d),(e) Two analyzed radiographs from drive pressures of 11.7 and 116.0 GPa, respectively. The higher-pressure drive results in densities that are 5 times higher than the lower-pressure case.

Figure 1(a) shows a schematic of the OMEGA EP laser platform. The targets consist of two tin foils oriented toward each other with an angle of 130° between the target normals. The tin foils have grooves carved into their interior surfaces, which traverse the entire foils and are $45\ \mu\text{m}$ deep with 60° opening angles. Figure 1(b) shows a picture of the assembled targets. The tin foils, which are $100\ \mu\text{m}$ thick, have $30\text{-}\mu\text{m}$ -thick plastic ablators on their front surfaces in order to increase laser drive efficiency; both the plastic and the tin foils have horizontal dimensions of $3.2\ \text{mm} \times 3.2\ \text{mm}$. Copper shields block the intense ablation-plasma emission from reaching the image plate diagnostic. A series of tin steps with known thicknesses on the target calibrates intensity on the image plate to areal density for the radiography diagnostic, and a grid on the target quantifies scale and resolution.

Two long-pulse lasers impinge on the plastic ablators with 8 ns square pulses of tunable energy, driving shock waves into the tin. $1800\ \mu\text{m}$ distributed phase plates are used on the drive lasers, ensuring large regions of planar drives on the targets. Figure 1(c) shows radiation hydrodynamics simulations performed using Ares [43] that mimic the experimental drive conditions to model pressure profiles within the tin foils at three different times during shock propagation for the sample case of an 11.7 GPa shock before release. A side view schematic of the groove to indicate dimensions is also overlaid on the plot. We perform independent velocity interferometry system for any reflector [44,45] measurements on single foil targets to quantify the shock pressure as a function of laser drive energy.

At a variable delay after the long-pulse laser turns on, a 500 J, 100 ps short-pulse laser heats a $20\text{-}\mu\text{m}$ -diameter titanium microwire, which generates a bright x-ray point source and projects a radiograph onto a shielded Fuji BAS-SR image plate placed within an OMEGA EP diagnostic port. The radiograph images along the axis perpendicular to the flow of both planar microjets with an image magnification of $\times 29.0$. Analysis of the radiographs suggests the imaging resolution is limited to $20\ \mu\text{m}$, the diameter of the microwire. Bremsstrahlung emission from the microwire dominates the spectral content of the x rays, highlighting the importance of the tin steps on the target for the calibration of image plate intensity to x-ray attenuation.

In order to quantify density measurements, we mask the inner surfaces of the tin with tantalum foils that are offset by $400\ \mu\text{m}$. The masks have dimensions of $3.2\ \text{mm} \times 1.1\ \text{mm} \times 125\ \mu\text{m}$ and are oriented perpendicularly to the groove direction. Pictures of the masks are shown in Fig. 1(b); for more details on the placement and performance of the masks, see Supplemental Material [46]. The masks limit the jetting material that reaches the diagnostic field of view such that the radiographs image the jets through an optical path of $1.0 \pm 0.1\ \text{mm}$.

Figures 1(d) and 1(e) show two analyzed radiographs of interacting jets from masked targets with (d) laser drives of 70 J and shock pressures of 11.7 GPa and (e) laser drives of 1200 J and shock pressures of 116.0 GPa. We observe densities of up to 30 and $150\ \text{mg cm}^{-3}$ for the cases of the lower drive and higher drive, respectively. The density relates linearly to the packing density of particles within the jetting material, otherwise known as the volume fraction. The microjet density we measure can be described as

$\rho = \Sigma_i m_i / V$, where $\Sigma_i m_i$ is the sum of the mass of all the particles i contained within the jetting volume V . Our radiographic uncertainties are larger than the relevant thermal expansion, so we assume particles at ambient density $\rho_0 = 7.31 \text{ g cm}^{-3}$, and we can write the density of the jet as $\rho = \rho_0 \Sigma_i v_i / V$. By definition, $\Sigma_i v_i / V = \rho / \rho_0$ is the volume fraction of jets. The volume fractions in the microjets reach up to 0.3% for the lower-pressure drive and 1.5% for the higher-pressure. Because of limitations in x-ray source reconstruction and 3D effects of the targets, we calculate up to 20% uncertainty in our density reconstruction.

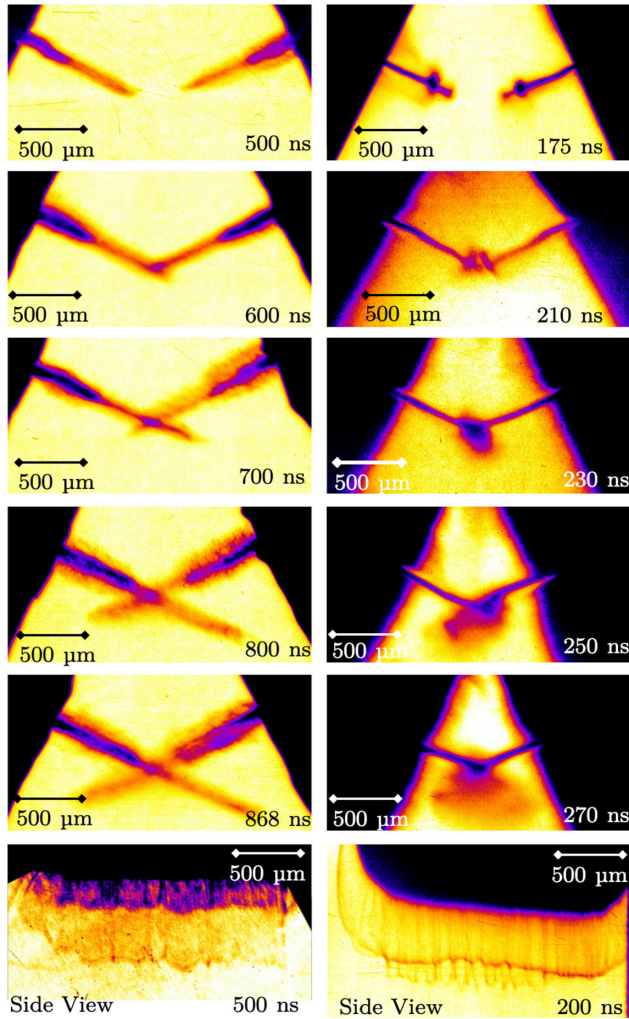


FIG. 2. Two sequences of radiographs of interacting planar tin ejecta microjets; the color scales with intensity on the image plate. The sequence on the left shows interaction between microjets with velocities of 2.2 km/s driven by 11.7 GPa shocks, and the sequence on the right shows jets traveling at 6.5 km/s from tin shocked at 116.0 GPa. A difference in interaction behavior is observed. Also shown at the bottom of the sequences are sample images of the side views of single unmasked planar jets.

The images in Figs. 1(d) and 1(e) hint at the differences in interaction behavior between the two pressures, but the differences are most strikingly seen in the time sequences of images shown in Fig. 2. The left side shows jets driven by shock pressures of 11.7 GPa, and the right side shows jets driven by 116.0 GPa shocks. The indicated times are referenced to the drive-laser turn-on. A difference in jet velocity of 0.5 km/s is observed between the left and right jets in the case of the lower-pressure drive, which may be attributed to imaging alignment or slightly different drive pressures ($< 2.8 \text{ GPa}$) on each foil; no difference in areal density is observed between the two jets, suggesting the potential drive difference does not result in altered jet compositions.

Analysis of the lower-pressure jets shows that the jets pass through each other unattenuated, maintaining the same velocity and density distributions. In comparison, the jets emerging from the higher-pressure shock generate a cloud of material upon interaction, suggesting a higher probability of particle collisions. Also shown at the bottom of each sequence in Fig. 2 are side-view images of single sheets of jetting material, each from a single unmasked target. The sheet view images demonstrate the inhomogeneities from the laser drive and the machining of the grooves. All images of interacting jets from the higher-pressure drive are from masked targets, while the lower-pressure drive images are masked only in the image shown in Fig. 1(d) (700 ns). Such interaction dynamics have never been observed before and, as such, offer important insights into the collisional behavior of microjets as a function of the volume fraction.

The jets also show different morphologies between the two shock pressures. Tin is a material known to melt over the pressure ranges explored in this experiment [47–50], and the mechanisms of jet formation are known to vary as a function of the material phase [41]. The lower-pressure jets show two regions of different densities due to shock interactions and spall-plane release [41]. The higher-pressure jets show regions of different widths, with higher-density 125- μm -thick bulbous regions leading the 50- μm -thick bulk jetting portions. The bulbous feature is believed to arise from a combination of material effects and the shape of the groove, which is not a triangle but a trapezoid with an 8 μm flat region at the vertex (see Supplemental Material [46]).

As part of these interaction studies, we aim to develop predictive capabilities for microjet interaction behavior for hydrodynamics simulations in Ares [43]. In principle, we would like to use a single simulation to model shock propagation through the sample, jet formation, material breakup, and the subsequent interactions. However, hydrocodes may lack the necessary physics, such as surface tension, to model jet breakup and can struggle to maintain the necessary computational resolution. As such, we are developing a multiphase particle-in-cell

approach as a more accurate reduced-order model of the postbreakup material, decoupling the simulations of the initial jet formation from the simulations of propagation and interaction, and we seek to understand the lowest-order model that can capture the interaction behavior we observe.

The simulations solve the two-way coupled transport equations for Lagrangian point particles in a Eulerian carrier fluid [51]. The code geometry mimics the experiment and injects teams of particles at experimentally measured volume fractions at the time of shock breakout from the tin. We assume a power-law distribution for the particle sizes based on previously published work from similar experimental geometries [25] and particle velocities distributed uniformly between a minimum and maximum value, tuned to match Ares hydrodynamics simulations of the jetting material [41] and the experimentally observed jet velocity. We set the jet width to the observed width of the bulk of the jetting material (50 μm).

The particles interact via a hard-sphere collisional model and treat collisions probabilistically, as described in Ref. [52]. Under this model, the probability of collision between two computational particles i and j in a computational cell is given by

$$P_{i,j} = \frac{\pi w_s (r_i + r_j)^2 |u_{i,j}| \Delta t}{V_{\text{cell}}}, \quad (1)$$

where w_s is the computational weight of the smaller particle derived from the particle size, r_i is the radius of particle i , $|u_{i,j}|$ is the relative velocity between particles i and j , Δt is the computational time step, and V_{cell} is the volume of the computational cell. If a collision occurs, a distribution is sampled to determine the impact parameter scaled by the radii of the two particles, $B \in [0, 1]$, and velocities of both particles are altered according to the scattering angle determined by B . Collisions are elastic and particles never coalesce or break up.

Simulations of two interacting microjets for the case of an 11.7 GPa shock exhibit the same unattenuated behavior that is observed in the experiments. Figure 3 shows simulated jet interactions from 116.0 GPa shocks. We characterize the spread of the interaction cloud for both the simulations and the data in the R and the S directions, as indicated in Fig. 3(a). The spread along R corresponds with the extent of the cloud from the center of the interaction point in the direction of jet propagation and assesses how much the jet slows in its original direction of propagation. We also quantify the vertical extent of the projection of the jets or cloud onto the center axis of symmetry, or the spread in the S direction. All spreads are defined as the widths between a volume fraction cutoff of 0.1% and are shown in Figs. 3(b) and 3(c). The hypothetical linear extents for unattenuated jets are depicted with orange dashed lines. For Fig. 3(c), the two points before interaction at 175 ns

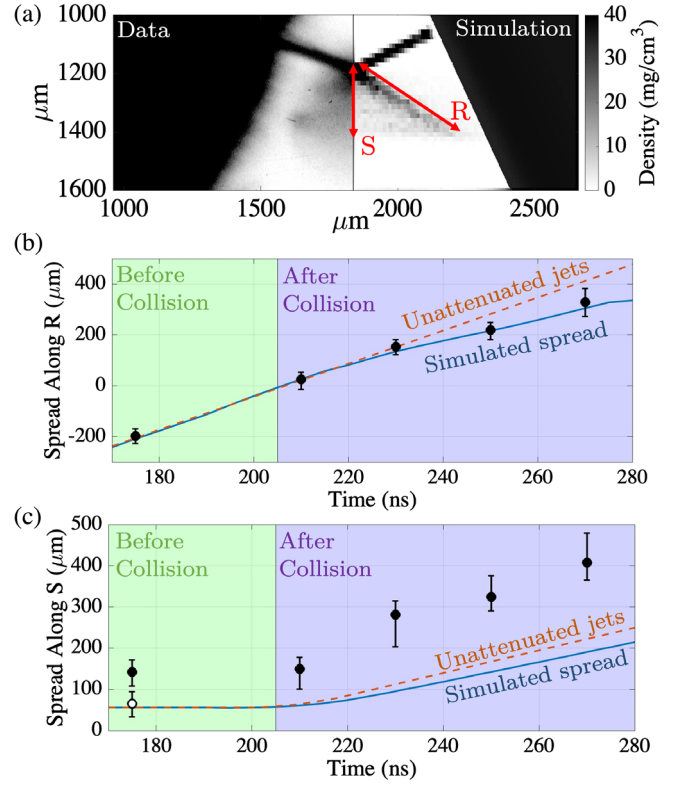


FIG. 3. High-pressure shock data and simulations for particle spread. (a) Density maps of the cloud for the data (left) and simulations (right). Spread as measured along the R and S directions is indicated for the case of the simulation. (b) The spread of the microjet cloud in the original direction of jet propagation as measured from the center point of the interaction, R direction, as observed in simulations (blue solid line) and experimentally (black data points). (c) The projection of jet vertical extent on the center axis of symmetry. The points before collision indicate the vertical extent of a single jet; the white point is the extent of the bulk of the jetting material, and the black point is the extent of small bulbous region near the front of the jet. The dashed orange lines in (b) and (c) represent the hypothetical linear extent of unattenuated jets. The simulation appears to capture the behavior of the spread in the R direction, but there is a mismatch in overall spread and postcollision velocity in the S direction.

indicate the vertical extent of a single jet in the bulk of the jetting material (white point) and in the bulbous feature (black point).

As shown in Fig. 3(b), the simulation captures the observed behavior of the jet speed slowing from 6.5 km/s to a velocity of 4.5 km/s after interaction; the collisions between particles result in altered mass-velocity distributions of the particles such that the particles travel in many directions, generating a cloud. However, in the case of the spread in S , Fig. 3(c) shows that the observed vertical extent of the cloud exceeds the spread predicted by the simulations. Lineouts of the spread in both the R and S directions for the data and simulations show similar

qualitative characteristics, with higher-density regions at the center of interaction followed by densities tapering with increased distance from the center. However, the simulations show an up-to-30% higher density at the center point of interaction, again suggesting that the simulations do not capture the full spread behavior.

The facts that the simulations assume the width of the bulk jetting material and do not capture the full extent of the cloud suggest that the increased width and density of the bulbous feature may account for the mismatch between observed and simulated spread. However, while simulations that assume the width and density of the bulbous feature do increase the extent of spread in S , they do not match the measured spread velocity of 4.0 km/s, instead reaching only 2.4 km/s. In addition, simulations that assume the width and density of the bulbous feature underpredict the spread in R , again failing to capture the observed interaction behavior.

One limitation of this collision model is that it assumes the jets are comprised of particles that can be described by hard spheres. While several experiments have shown that micron-sized particles comprise microjets, it is reasonable to think that the phases and particle sizes may differ between an 11.7 and 116.0 GPa shock drive and that the resulting jets may behave differently upon interaction. However, the phase of the jets is unknown, as strain rates exceeding $1 \times 10^7 \text{ s}^{-1}$ and plastic work dissipation may lead to localized melting phenomena or phase transition kinetics, and cooling may lead to solid particles [53,54]; in addition, hydrodynamics simulations suggest that jets generated by shock pressures below which tin is known to melt may contain fractions of melted material. Phase effects, as well as breakup and conglomeration, may contribute to the observed differences between the experiments and the simulations. Another contributing factor could be inhomogeneities in planarity of the jet.

More experiments are needed to understand both the collision model deficiencies and the onset of interaction behavior as a function of shock pressure. Increasing the groove opening angle and depth can increase the jet density and speed, respectively, for a given shock pressure, and sample materials that melt at higher temperatures than tin would allow for increased jet density with increasing shock pressure without increasing the fraction of melted material in the jet. This would allow for comparisons of jet interactions at different densities and velocities without different material phases. Techniques such as x-ray diffraction may be used to quantify melted material fraction in the jets, and small angle x-ray scattering or holography may be used to probe particle size distributions; single-particle experiments are also proposed as a way to quantify collision elasticity. While uncertainties of the driving physics remain, these recent experiments provide the first data on interacting ejecta microjet behavior and a novel methodology to observe the interactions of high-velocity

particle-laden flows, which opens many more avenues for detailed study.

We thank Channing Huntington for his early guidance on the project, as well as Russ Wallace and the target fabrication team for extensive target development efforts. This work was performed under the auspices of the U.S. Department of Energy by Lawrence Livermore National Laboratory under Contract No. DE-AC52-07NA27344 and supported by Laboratory Directed Research and Development (LDRD) Grant No. 18-ERD-060. This material is also based upon work supported by the Department of Energy National Nuclear Security Administration under Grant No. DE-NA0003856, the University of Rochester, and the New York State Energy Research and Development Authority. The support of DOE does not constitute an endorsement by DOE of the views expressed in this paper.

*Corresponding author.
saunders15@llnl.gov

- [1] M. Lambrechts and A. Johansen, *Astron. Astrophys.* **544**, A32 (2012).
- [2] M. Lambrechts, A. Morbidelli, S. A. Jacobson, A. Johansen, B. Bitsch, A. Izidoro, and S. N. Raymond, *Astron. Astrophys.* **627**, A83 (2019).
- [3] A. Johansen and M. Lambrechts, *Annu. Rev. Earth Planet Sci.* **45**, 359 (2017).
- [4] B. Bitsch, M. Lambrechts, and A. Johansen, *Astron. Astrophys.* **582**, A112 (2015).
- [5] J. Chambers, *Icarus* **233**, 83 (2014).
- [6] H. Katsuragi and J. Blum, *Phys. Rev. Lett.* **121**, 208001 (2018).
- [7] J. Blum, *Space Sci. Rev.* **214**, 52 (2018).
- [8] E. W. Saw, R. A. Shaw, S. Ayyalasomayajula, P. Y. Chuang, and A. Gylfason, *Phys. Rev. Lett.* **100**, 214501 (2008).
- [9] K. Gustavsson, S. Vajedi, and B. Mehlig, *Phys. Rev. Lett.* **112**, 214501 (2014).
- [10] M. Gibert, H. Xu, and E. Bodenschatz, *J. Fluid Mech.* **698**, 160 (2012).
- [11] J. Wu, J. Binbo, J. Chen, and Y. Yang, *Adv. Powder Technol.* **20**, 62 (2009).
- [12] E. Calzavarini, M. Cencini, D. Lohse, and F. Toschi (International Collaboration for Turbulence Research), *Phys. Rev. Lett.* **101**, 084504 (2008).
- [13] Z. Warhaft, *Fluid Dyn. Res.* **41**, 011201 (2009).
- [14] R. A. Shaw, *Annu. Rev. Fluid Mech.* **35**, 183 (2003).
- [15] T. Matsumoto, K. Dobashi, and T. Shimoikura, *Astrophys. J.* **801**, 77 (2015).
- [16] J. L. Sinclair and R. Jackson, *AIChE J.* **35**, 1473 (1989).
- [17] Y. Lian and K. Xu, *J. Comput. Phys.* **163**, 349 (2000).
- [18] R. D. Richtmyer, *Commun. Pure Appl. Math.* **13**, 297 (1960).
- [19] E. E. Meshkov, *Izv. Akad. Nauk SSSR, Mekh. Zhidk. Gaza* **5**, 151 (1969).
- [20] K. O. Mikaelian, *Phys. Rev. Lett.* **80**, 508 (1998).
- [21] K. O. Mikaelian, *Phys. Rev. E* **81**, 016325 (2010).

- [22] A. B. Georgievskaya and V. A. Raevsky, *J. Dyn. Behav. Mater.* **3**, 321 (2017).
- [23] J. R. Asay, L. P. Mix, and F. C. Perry, *Appl. Phys. Lett.* **29**, 284 (1976).
- [24] M. M. Schauer, W. T. Buttler, D. K. Frayer, M. Grover, S. K. Monfared, D. S. Sorenson, G. D. Stevens, and W. D. Turley, *J. Dyn. Behav. Mater.* **3**, 217 (2017).
- [25] D. S. Sorenson, R. W. Minich, J. L. Romero, T. W. Tunnell, and R. M. Malone, *J. Appl. Phys.* **92**, 5830 (2002).
- [26] O. Durand and L. Soulard, *J. Appl. Phys.* **114**, 194902 (2013).
- [27] W. T. Buttler, D. M. Oró, D. L. Preston, and K. O. Mikaelian, *J. Fluid Mech.* **703**, 60 (2012).
- [28] F. Wu, Y. Zhu, X. Li, P. Wang, Q. Wu, and H. Wu, *J. Appl. Phys.* **125**, 185901 (2019).
- [29] O. Durand and L. Soulard, *J. Appl. Phys.* **111**, 044901 (2012).
- [30] C. S. Speight, L. Harper, and V. S. Smeeton, *Rev. Sci. Instrum.* **60**, 3802 (1989).
- [31] W. T. Buttler, M. B. Zellner, R. T. Olson, P. A. Rigg, R. S. Hixson, J. E. Hammerberg, A. W. Obst, J. R. Payton, A. Iverson, and J. Young, *J. Appl. Phys.* **101**, 063547 (2007).
- [32] T. de Rességuier, G. Prudhomme, C. Roland, E. Brambrink, D. Loison, B. Jodar, E. Lescoute, and A. Sollier, *J. Appl. Phys.* **124**, 065106 (2018).
- [33] G. Prudhomme, J.-E. Franzkowiak, T. de Rességuier, E. Brambrink, C. Roland, D. Loison, E. Lescoute, and A. Sollier, *AIP Conf. Proc.* **1979**, 080010 (2018).
- [34] W. S. Vogan, W. W. Anderson, M. Grover, J. E. Hammerberg, N. S. P. King, S. K. Lamoreaux, G. Macrum, K. B. Morley, P. A. Rigg, G. D. Stevens, W. D. Turley, L. R. Veaser, and W. T. Buttler, *J. Appl. Phys.* **98**, 113508 (2005).
- [35] A. M. Saunders, S. J. Ali, H.-S. Park, J. Eggert, F. Najjar, C. Huntington, T. Haxhimali, B. Morgan, Y. Ping, and H. G. Rinderknecht, *AIP Conf. Proc.* **2272**, 120025 (2020).
- [36] M. B. Zellner, W. Vogan McNeil, G. T. Gray, D. C. Huerta, N. S. P. King, G. E. Neal, S. J. Valentine, J. R. Payton, J. Rubin, G. D. Stevens, W. D. Turley, and W. T. Buttler, *J. Appl. Phys.* **103**, 083521 (2008).
- [37] F. J. Cherne, J. E. Hammerberg, M. J. Andrews, V. Karkhanis, and P. Ramaprabhu, *J. Appl. Phys.* **118**, 185901 (2015).
- [38] Y. Chen, H. Hu, T. Tang, G. Ren, Q. Li, R. Wang, and W. T. Buttler, *J. Appl. Phys.* **111**, 053509 (2012).
- [39] P. Andriot, P. Chapron, and F. Olive, *AIP Conf. Proc.* **78**, 505 (1982).
- [40] C. F. McMillan, in *Proceedings of the 17th International Congress on High Speed Photography and Photonics*, edited by D. Hollingworth and M. W. McDowell, International Society for Optics and Photonics (SPIE, Bellingham, WA, 1987), Vol. 0674, pp. 289–300.
- [41] K. K. Mackay, F. M. Najjar, S. J. Ali, J. H. Eggert, T. Haxhimali, B. E. Morgan, H. S. Park, Y. Ping, H. G. Rinderknecht, C. V. Stan, and A. M. Saunders, *J. Appl. Phys.* **128**, 215904 (2020).
- [42] J. H. Kelly *et al.*, *J. Phys. IV* **133**, 75 (2006).
- [43] R. M. Darlington, T. L. McAbee, and G. Rodrigue, *Comput. Phys. Commun.* **135**, 58 (2001).
- [44] L. M. Barker and R. E. Hollenbach, *J. Appl. Phys.* **43**, 4669 (1972).
- [45] P. M. Celliers, D. K. Bradley, G. W. Collins, D. G. Hicks, T. R. Boehly, and W. J. Armstrong, *Rev. Sci. Instrum.* **75**, 4916 (2004).
- [46] See Supplemental Material at <http://link.aps.org/supplemental/10.1103/PhysRevLett.127.155002> for more information about the target geometry, the methods used for density reconstruction from radiography images, and hydrodynamics simulations of the microjetting process.
- [47] A. Lazicki, J. R. Rygg, F. Coppari, R. Smith, D. Fratanduono, R. G. Kraus, G. W. Collins, R. Briggs, D. G. Braun, D. C. Swift, and J. H. Eggert, *Phys. Rev. Lett.* **115**, 075502 (2015).
- [48] A. Salamat, G. Garbarino, A. Dewaele, P. Bouvier, S. Petitgirard, C. J. Pickard, P. F. McMillan, and M. Mezouar, *Phys. Rev. B* **84**, 140104(R) (2011).
- [49] R. Briggs, D. Daisenberger, A. Salamat, G. Garbarino, M. Mezouar, M. Wilson, and P. F. McMillan, *J. Phys. Conf. Ser.* **377**, 012035 (2012).
- [50] C. Mabire and P.-L. Hereil, *J. Phys. IV* **10**, Pr9 (2000).
- [51] J. A. McFarland, W. J. Black, J. Dahal, and B. E. Morgan, *Phys. Fluids* **28**, 024105 (2016).
- [52] A. A. Amsden, P. J. O'Rourke, and T. D. Butler, KIVA-II: A computer program for chemically reactive flows with sprays, Los Alamos National Laboratory, technical report, 1989.
- [53] D. Lassila, D. Nikkel, R. Kershaw, and W. Walters, in *Proceedings of the American Society of Mechanical Engineers Pressure Vessels and Piping Conference, 1996* (American Society of Mechanical Engineers, New York, 1996).
- [54] W. C. Uhlig and C. R. Hummer, *Proc. Eng.* **58**, 48 (2013).